

Fall 2010

# Electron transitions and propagation characteristics of dipolarization fronts observed by cluster

Jinyoung Park

*University of New Hampshire, Durham*

Follow this and additional works at: <https://scholars.unh.edu/thesis>

---

## Recommended Citation

Park, Jinyoung, "Electron transitions and propagation characteristics of dipolarization fronts observed by cluster" (2010). *Master's Theses and Capstones*. 592.

<https://scholars.unh.edu/thesis/592>

This Thesis is brought to you for free and open access by the Student Scholarship at University of New Hampshire Scholars' Repository. It has been accepted for inclusion in Master's Theses and Capstones by an authorized administrator of University of New Hampshire Scholars' Repository. For more information, please contact [nicole.hentz@unh.edu](mailto:nicole.hentz@unh.edu).

**ELECTRON TRANSITIONS AND PROPAGATION  
CHARACTERISTICS OF DIPOLARIZATION  
FRONTS OBSERVED BY CLUSTER**

BY

JINYOUNG PARK

B. S., Chung-nam National University, 2004

M. S., Chung-nam National University, 2006

THESIS

Submitted to the University of New Hampshire  
in partial fulfillment of  
the requirements for the Degree of

Master of Science

in

Physics

September 2010

UMI Number: 1487007

All rights reserved

**INFORMATION TO ALL USERS**

The quality of this reproduction is dependent upon the quality of the copy submitted.

In the unlikely event that the author did not send a complete manuscript and there are missing pages, these will be noted. Also, if material had to be removed, a note will indicate the deletion.



UMI 1487007

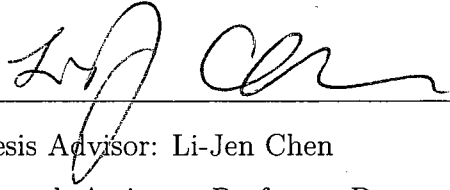
Copyright 2010 by ProQuest LLC.

All rights reserved. This edition of the work is protected against unauthorized copying under Title 17, United States Code.



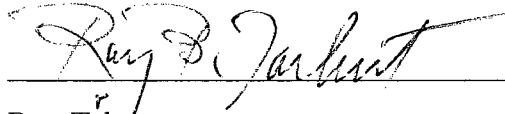
ProQuest LLC  
789 East Eisenhower Parkway  
P.O. Box 1346  
Ann Arbor, MI 48106-1346

This thesis has been examined and approved.



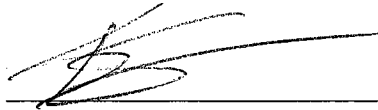
---

Thesis Advisor: Li-Jen Chen  
Research Assistant Professor, Department of Physics  
Research Assistant Professor, Space Science Center  
Institute for the Study of Earth, Oceans, and Space



---

Roy Tqbert  
Professor, Department of Physics  
Professor, Space Science Center  
Institute for the Study of Earth, Oceans, and Space



---

Karl Slifer  
Assistant Professor, Department of Physics

Aug 24 . 2010

---

Date

# ACKNOWLEDGMENTS

I would like to express my appreciation and thanks to my advisor Li-Jen Chen for her help with all the details of my research, for her friendship, and for her constant reminders to walk at my own pace and enjoy the journey. I would also like to thank my committee members for their contributions to this study: Roy Torbert for his comments on the observational aspect of this study and Karl Slifer for his comments and suggestions on the general and basic aspects of this study.

I am very grateful to all of my colleagues who have helped me with the Cluster observation data, especially Hans Vaith who contributed the FGM and the EDI data, Bertrand Lefebvre who taught me how to plot the PEACE electron distribution array and Christopher Mouikis who helped me to analyze the CIS data.

I would also like to thank my fellow graduate students in the physics department who I took classes with and who shared their knowledge and enthusiasm of space science with me. Together, we were able to go through all assignments and projects and also spent periods of fun and relaxation sometimes after the exams.

In addition, I would like to give many thanks to my family and friends who always cheer me and support my way. In particular, I am very grateful to my husband, Philip, for his warm and active support of my work and for his sincere love in my life.

Finally, I am very thankful to my God who allows me all of these accomplishments and who gave me all the good people, friendship and love in my life.

# TABLE OF CONTENTS

ACKNOWLEDGMENTS . . . . .	iii
LIST OF TABLES . . . . .	v
LIST OF FIGURES . . . . .	vi
ABSTRACT . . . . .	vii
<b>1 INTRODUCTION</b>	<b>1</b>
<b>2 THE CLUSTER SPACECRAFT</b>	<b>12</b>
2.1 Data sets used in this study . . . . .	12
<b>3 RESULTS</b>	<b>17</b>
3.1 Selection criteria . . . . .	17
3.2 Example of the DPFs on 20051003 . . . . .	18
3.3 Electron transitions at the DPFs . . . . .	18
3.4 Propagation characteristics of the DPFs . . . . .	21
<b>4 DISCUSSION AND SUMMARY</b>	<b>33</b>
<b>BIBLIOGRAPHY</b>	<b>38</b>

## List of Tables

2.1	Summary of the measurement range and the time resolution of the Cluster instruments . . . . .	15
3.1	9 Dates of DPF events with the position of spacecraft 1 . . . . .	24
3.2	Minimum Variance Analysis results on 20051003 and 20060903 . . .	24

## List of Figures

1-1	Schematic of the magnetotail . . . . .	5
1-2	Two reconnection related models for the generation of DPFs . . . . .	6
1-3	The relationship between the DPFs and the aurora breakups . . . . .	7
1-4	Three properties of the DPF . . . . .	8
1-5	Change of the electron flux at a dipolarization structure . . . . .	9
1-6	Electron transition at the DPF observed by THEMIS . . . . .	10
1-7	Earthward propagation of the DPF observed by THEMIS . . . . .	11
2-1	Schematic of the Cluster polar orbit . . . . .	16
3-1	Positions of four spacecraft for all 9 dates of event in X-Y plane and in X-Z (bottom) planes (GSM) . . . . .	25
3-2	Example of the DPFs on 20051003 . . . . .	26
3-3	Samples of electron distribution functions from PEACE . . . . .	27
3-4	Transitions of the thermal and the superthermal electrons on 20051003	28
3-5	Electron transitions at the second DPF on 20051003 . . . . .	29
3-6	Three types of $B_z$ rise with electron transitions . . . . .	30
3-7	Propagation characteristics of the DPF on 20051003 . . . . .	31
3-8	Propagation characteristics of the DPF on 20060903 . . . . .	32
4-1	The generation of the DPF from two fluid simulation . . . . .	36
4-2	Magnetic field lines and the current density from 2-D PIC simulation	37



# ABSTRACT

## ELECTRON TRANSITIONS AND PROPAGATION CHARACTERISTICS OF DIPOLARIZATION FRONTS OBSERVED BY CLUSTER

by

Jinyoung Park

University of New Hampshire, September, 2010

This thesis describes electron transitions at the dipolarization fronts (DPFs) observed by Cluster using high time-resolution data. The sharp electron transitions occur within the rising phase of the magnetic field component  $B_z$  normal to the magnetotail current sheet. The electron transitions provide a new constraint on the DPFs generation models that are related to reconnection. A sudden  $B_z$  rise without a small dip prior to the increase was observed suggesting that tearing instabilities in the reconnection exhaust may not be required for the generation of DPFs. Based on timing and minimum variance analysis, the DPFs are found to have a curved structure and propagate earthward. The results in this study are consistent with DPFs being the injection fronts from the reconnection exhaust.

# CHAPTER 1

## INTRODUCTION

A dipolarization front (DPF) is a steep increase of the magnetic field component normal to the magnetotail current sheet. When magnetic reconnection occurs in the magnetotail, the heated and accelerated plasma is produced as the reconnection exhaust and injected toward the Earth. Dipolarization fronts (DPFs) can be interpreted as the magnetic flux pileup due to the fast earthward injection flows from the reconnection. DPFs are thought to provide the free energy to generate the field-aligned currents of the substorm current wedge that eventually produces the aurora, and therefore are closely associated with the auroral breakup (Hesse and Birn, 1991).

The magnetotail current sheet is one of the regions in the Earth's magnetosphere produced by an interaction between the solar wind and the Earth dipole. Figure 1-1 shows a schematic of the magnetosphere. In this study, the Geocentric Solar Magnetospheric (GSM) coordinate system is used. Based on the Geocentric Solar Magnetospheric (GSM) coordinate system, the x component of the magnetic field ( $B_x$ ) is positive above the current sheet and negative below the current sheet. The X-axis in GSM is positive toward the Earth and the Sun. The Y-axis in GSM is perpendicular to the Earth's dipole and positive toward dusk. The Z-axis in GSM is the cross product of X and Y-axes. The properties of DPFs include their fast earthward plasma flow, a decrease of ion density as well as a sharp rise of z component of the magnetic field normal to the magnetotail current sheet, preceded by a small decrease in  $B_z$ . There are many scenarios attempting to explain the generation of DPFs. Based on the scientific literature, the magnetic reconnection which produces the heated and accelerated plasma injections is consistent with previously observed DPFs. Information on the heated and accelerated injection as well as the

magnetic flux pile up allow to draw conclusion on all three properties mentioned above (i.e. fast earthward plasma flow, a decrease of ion density, a sharp rise of  $B_z$ ). In addition,  $|B_z|$  values are independent of the radial distance from the Earth. This supports the reconnection related scenarios for the generation of the DPFs.

Two reconnection related models which show the generation of the DPFs are presented in Figure 1-2. One is a two-fluid simulation shown in Figure 1-2(a). In this figure, the Earth is located on the left side. The red arrows indicate the direction of the magnetic field. The time and space scales are normalized by inverse of ion gyro frequency and ion skin depth. Figure 1-2(a) shows the magnetic X-lines with distributions of  $J_y$  in gray scale and with contours of the magnetic potential. After reconnection, there is a magnetic island in the exhaust region and a bipolar  $B_z$  structure is observed on the virtual spacecraft in the model. The other simulation is 2-D particle-in-cell (PIC) model presented in Figure 1-2(b). Here, the Earth is located on the right side of the figure. The black arrows indicate the direction of the magnetic field. The top panel of Figure 1-2(b) shows the magnetic field lines and the color-coded current density at the moment  $\Omega_i t = 12$ . The cuts along  $z=0$  at seven different times to show the  $B_z$  profiles are plotted in the bottom panel of Figure 1-2(b). 2-D PIC model produces the asymmetry of south to north  $B_z$  profile produced by reconnection. However, none of the simulations account for electron data. Our Cluster observations provide a new constraint of the generation of the DPFs using electron data of high time resolution. These models are discussed in further detail in Discussion section.

The generation of DPFs are closely associated with initiations of substorms. Typically, the DPFs are associated with a decrease in the cross-tail current in the near-Earth region (Hesse and Birn, 1991). The disruption of the cross-tail current in the magnetotail is believed to be closely associated with the occurrence of the auroral brightening (Hesse and Birn, 1991; Volwerk et al., 2008). Fillingim et al. (2001) present the relationship between the auroral intensity and the sudden rises of  $B_z$  observed by WIND around  $x \sim 10 R_e$ . As shown in Figure 1-3, with an increase in  $B_z$  the aurora intensity increases and the aurora is expanded in latitude. In addition, the earthward ion flow (positive  $V_x$ ) as well as the superthermal ion fluxes

(>20 keV) rise simultaneously. Studying the characteristics of DPFs therefore helps to understand substorm initiations.

Figure 1-4 presents three properties of the DPFs observed by Geotail (Ohtani et al., 2004). In the figure, each curve represents a number of events averaged to make profiles of the ion velocity, values of  $B_z$  and the ion density on different locations from  $x = -5$  to  $-31 R_e$ . Numbers in parenthesis represent the number of the DPFs events. Fast earthward ion flows at the sudden  $B_z$  rise are shown in the first and second panels of Figure 1-4, respectively. The bottom panel shows that the ion densities suddenly decrease when  $B_z$  increases. It should be noted that the small dip of  $B_z$  does not go through zero. This Geotail observation only consider the ion data at the DPFs.

Electrons carry key information about the magnetic topology and the ongoing dynamics. Measurements of electrons should therefore provide critical information about the candidate DPF generation mechanisms. Previous observations of DPFs have primarily focused on correlating ion bulk parameters with magnetic field variations to understand the mass and momentum transport aspects of DPFs (Ohtani et al., 2004). The few studies which included electron data indicated that hot and tenuous electrons are observed around the time when DPFs are observed (Lui et al., 1992; Runov et al., 2009). Figure 1-5 presents the electron transitions at the DPF,  $\sim 23:14:45$  UT with three different energy channels. The electron transitions are energy dependent, for example, the electron fluxes in the channels of 0.58 keV to 4.9 keV suddenly decrease at the increase of  $B_H$  ( $B_H$  is parallel to the Earth's dipole in  $VDH$  coordinate system). However the high energy of electrons above 15 keV increase at the DPF. Lui et al. (1992) reported the correlation between electron transitions and the DPFs but the study was not able to resolve sharp  $B_z$  transition with electron data. According to Runov et al. (2009), the electron energy flux changed with a sudden increase of  $B_z$ . Figure 1-6 (a) shows a typical DPF (sudden increase of  $B_z$ , decreased of ion density and increase of ion velocity) observed by THEMIS with 3 components of the magnetic field, ion and electron energy spectrograms as well as ion density and ion velocity versus time. The time span in which the rise of  $B_z$  occurs is only less than 2 s (Figure 1-6 (b)). However, electron data used for

Figure 1-6 (a) is not capable of providing sufficient information about the increase in  $B_z$  due to the fact that the electron time resolution is 3 s. In this thesis, electron data with sufficient time-resolution from the four-spacecraft mission named Cluster is used to examine the electron transitions at the DPFs.

Several studies have been undertaken on the direction and speed of the propagation of DPFs. Nakamura et al. (2002) examined the propagation direction and speed of DPF observed by the Cluster spacecraft using a timing and a minimum variance analysis. From these analyses, the planar structure of the DPF propagated earthward with a speed of  $\sim 77 \text{ km/s}$  are presented. Runov et al. (2009) described the earthward propagation of DPFs over a distance of more than  $10 R_e$  on THEMIS observations. Figure 1-7 shows the spacecraft position in X-Y plane and X-Z plane in (a) and the  $B_z$  profiles observed from each probe (b). However, in this study the spacecraft alignment is linear and only one point observation from each location is shown. Hence it did not describe the three-dimensional propagation. In this thesis the direction and speed of propagation is considered by using multi-point analysis from Cluster.

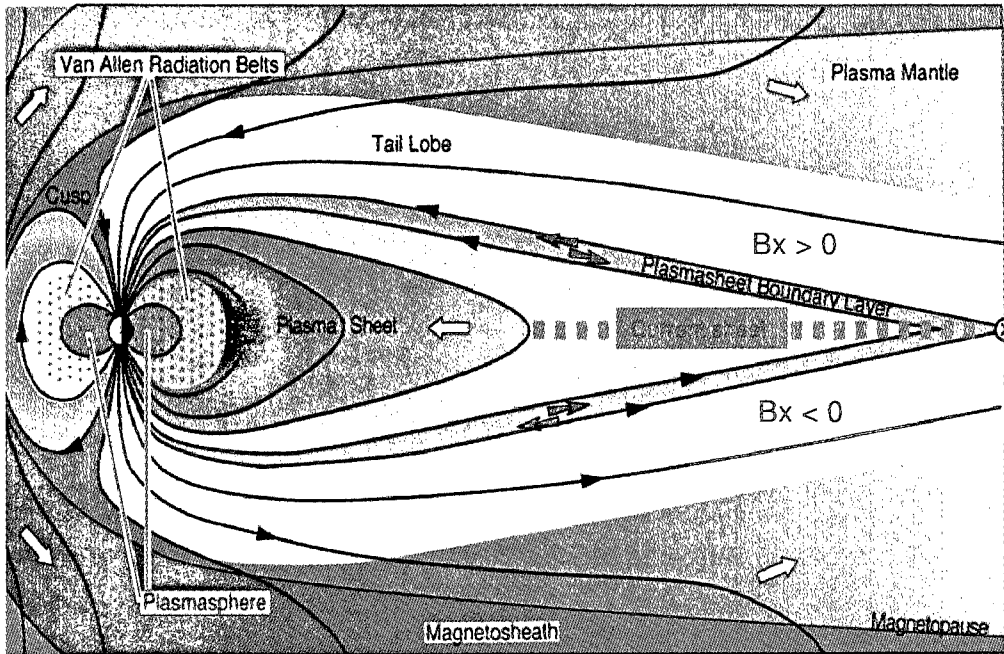


Figure 1-1: **Schematic of the magnetotail.** There are many regions in the Earth's magnetosphere. This study focuses on the current sheet in order to understand the generation of the DPFs. Based on the Geocentric Solar Magnetospheric (GSM) coordinate system,  $B_x$  is positive (negative) above (below) the current sheet.

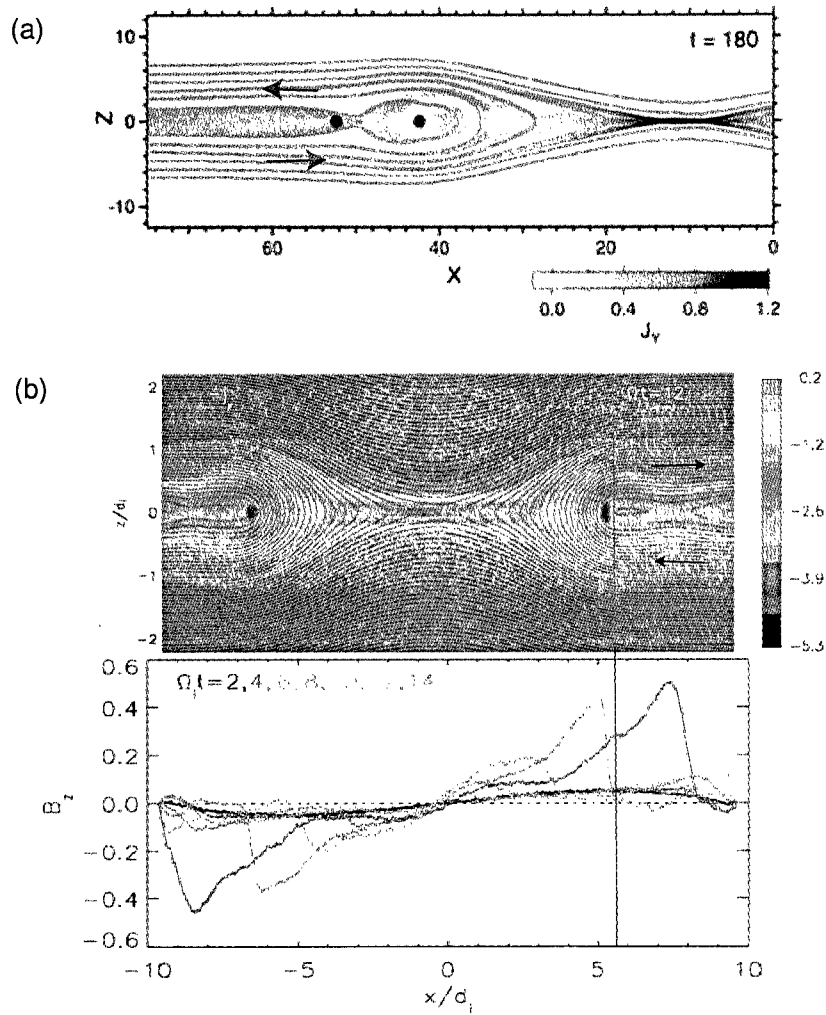


Figure 1-2: **Two reconnection related models for the generation of DPFs.** The two-fluid simulation is shown in (a) (Ohtani et al., 2004). The Earth is located on the left side of the figure. Magnetic X-lines with distributions of  $J_y$  in gray scale and with contours of the magnetic potential are plotted in (a). The 2-D PIC simulation is presented in (b) (Sitnov et al., 2009). The earth is located on the right side of figure. The magnetic field lines and the color-coded current density at the moment  $\Omega_i t = 12$  are shown in the top panel, while the cuts along  $z=0$  at different times to show the  $B_z$  profiles are shown in the bottom panel.

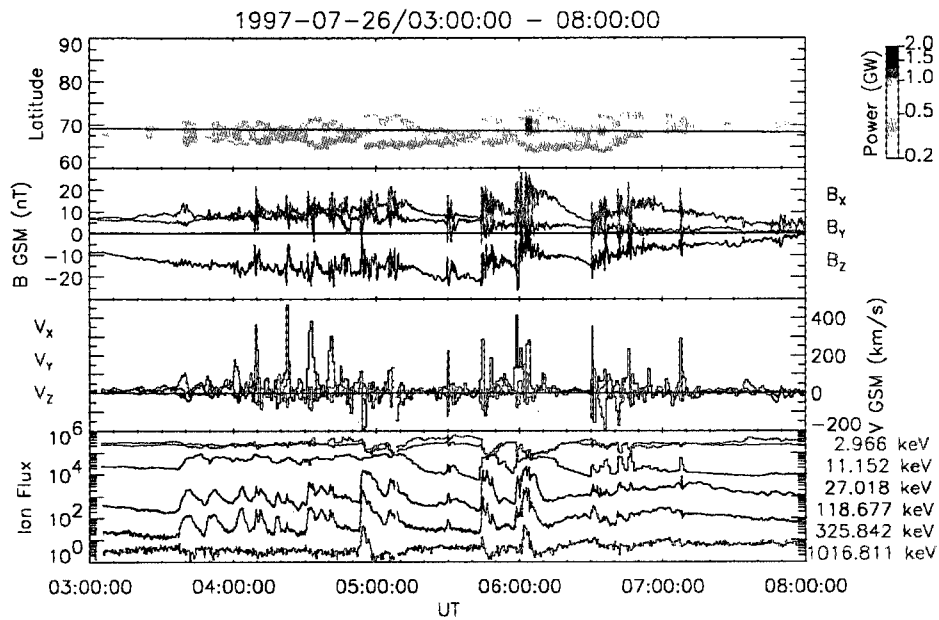


Figure 1-3: **The relationship between the DPFs and the aurora breakups (Fillingim et al., 2001).** The first panel indicates the auroral emission power in ultraviolet (UV) range with the latitude shown on the y axis. The second panel presents all three components of the magnetic field. The third panel shows three components of the ion flow and the last panel shows the ion flux.



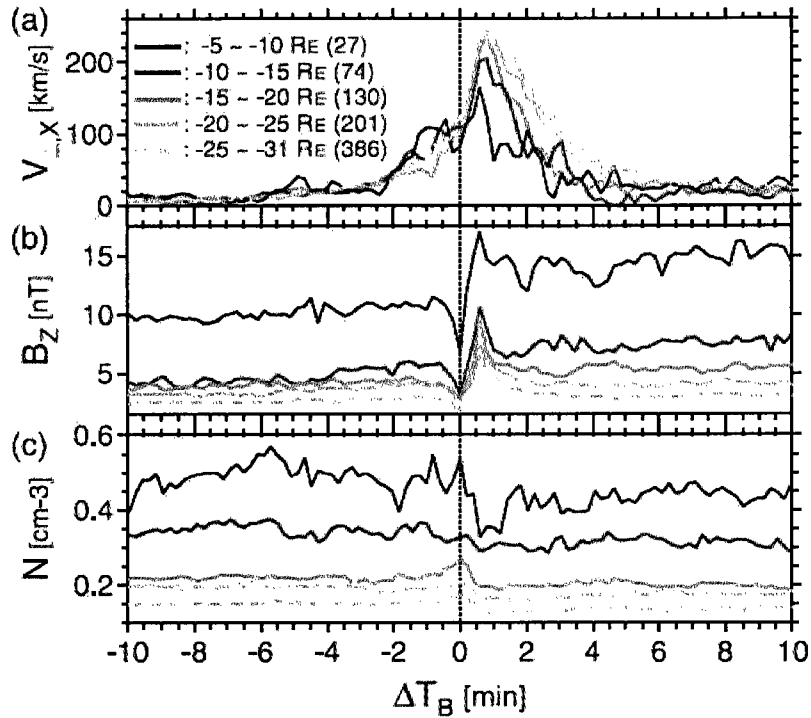


Figure 1-4: **Three properties of the DPF (Ohtani et al., 2004).** The top panel shows the ion flow in x direction, while the second panel presents the z component of magnetic field. The bottom panel shows the ion density. In all panels, five lines present average values of DPFs events observed from  $x = -5$  to  $-31 R_e$  (the numbers in parenthesis indicate the counts of events being averaged). The vertical dotted line at  $\Delta T_B = 0$  indicate the point in time when a small  $B_z$  dip is observed.

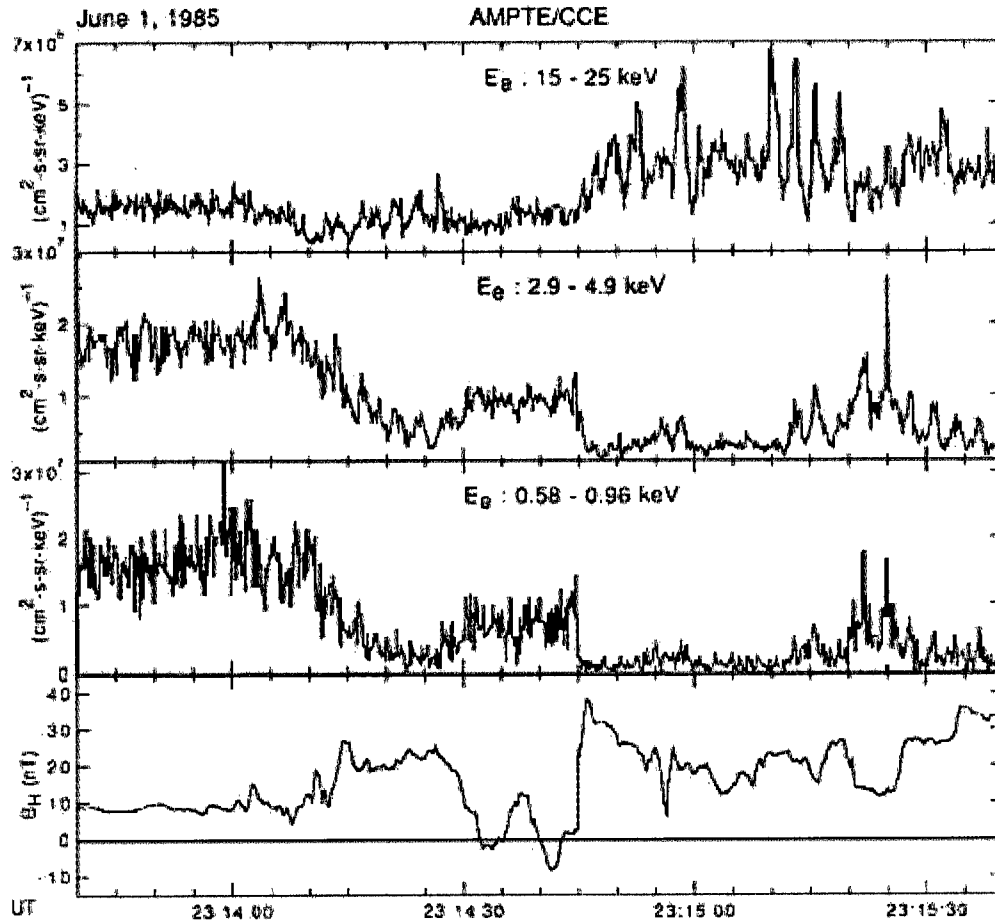


Figure 1-5: Change of the electron flux at a dipolarization structure (Lui et al., 1992). The electron flux in three energy channels, and the  $B_H$  component of the magnetic field (parallel to the Earth's dipole) are shown in the top to the bottom panels, respectively.

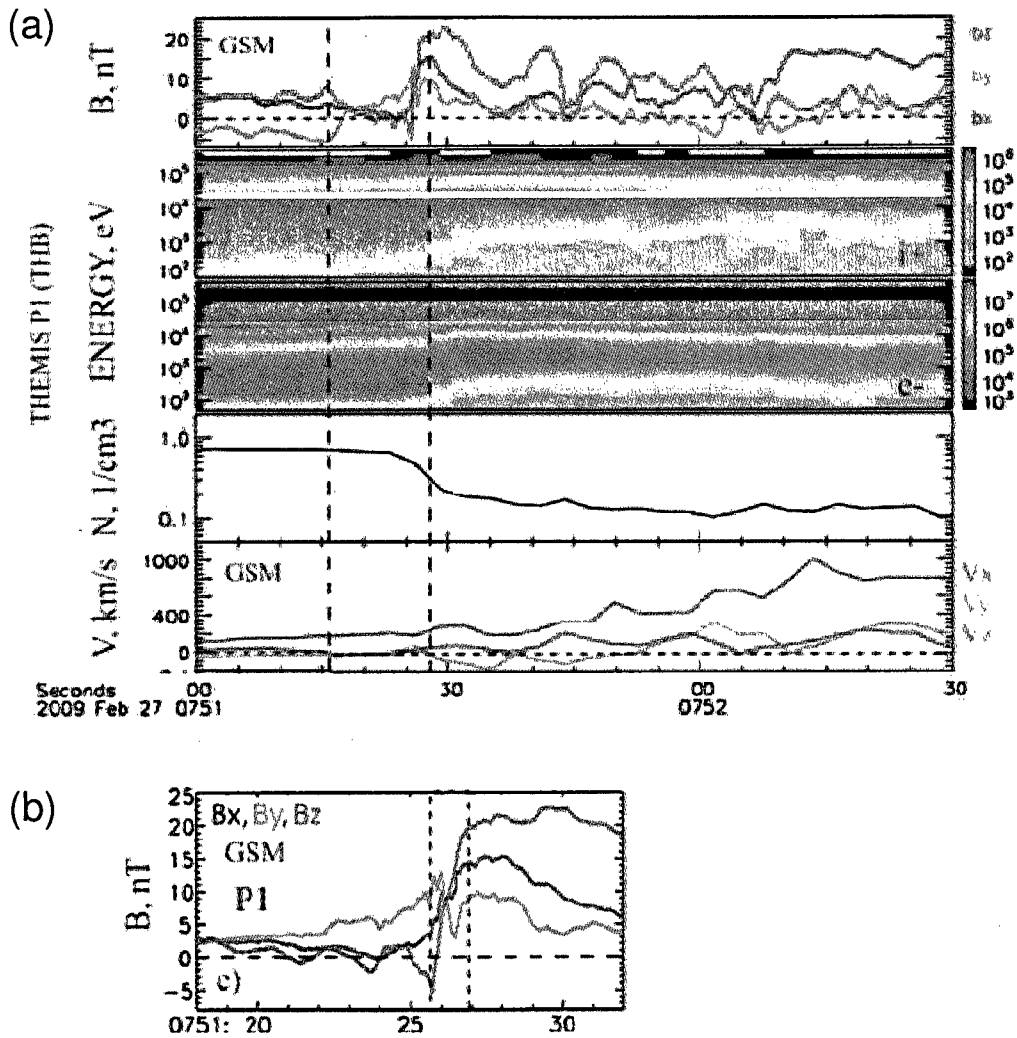


Figure 1-6: Electron transition at the DPF observed by THEMIS (Runov et al., 2009). The time on the x axis is plotted versus the three components of the magnetic field including the ion and electron energy spectrograms, the ion density, and the ion velocity (a). A zoom-in view of  $B_z$  ramp is presented in (b).

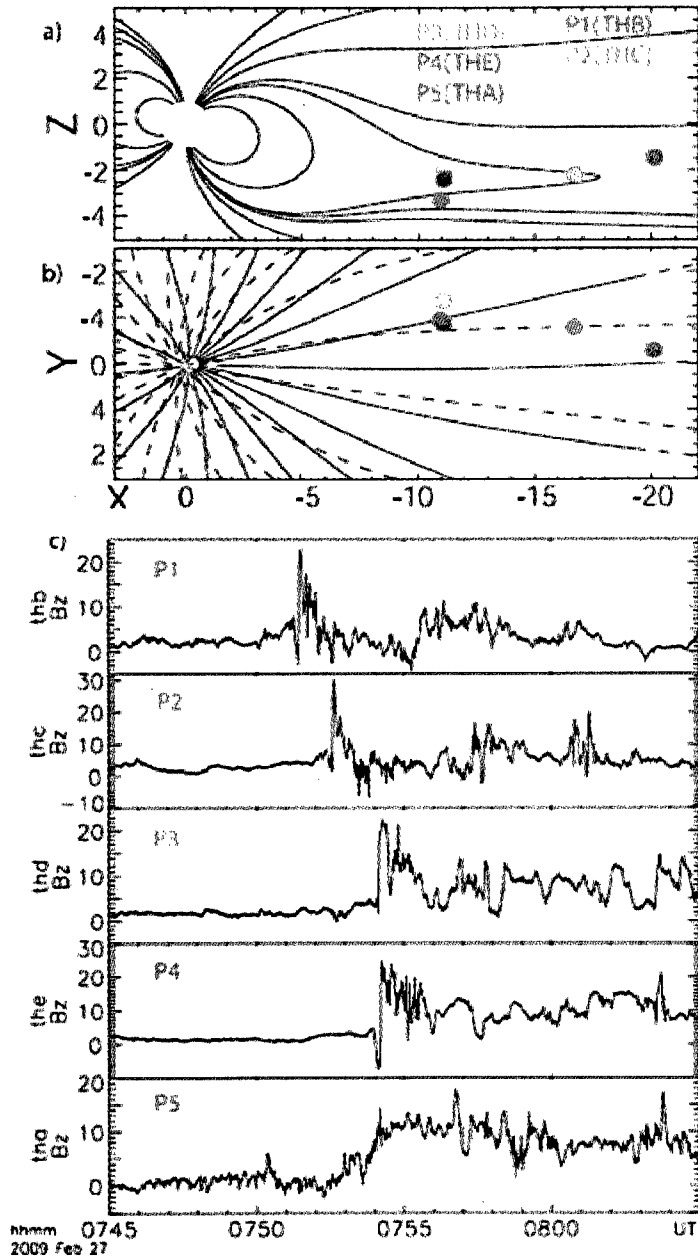


Figure 1-7: Earthward propagation of the DPF observed by THEMIS (Runov et al., 2009). All THEMIS spacecraft positions are projected in the X-Z plane (a) and X-Y plane (b). The colored dots denote the spacecraft positions. The z component of the magnetic field measured from each probe is plotted in (c).

# CHAPTER 2

## THE CLUSTER SPACECRAFT

The Cluster mission is designed with four spacecraft flying in close approximation to each other in tetrahedral configuration. In order to allow for measurements of three-dimensional structures, at least 4 spacecraft are needed. The orbit of Cluster is designed as a polar orbit, with a perigee of  $4 R_e$  and an apogee of  $19.6 R_e$ . The aim of the mission is to investigate the small-scale structure of the Earth's plasma environment, such as the global magnetotail dynamics, cross-tail currents, and the formation and dynamics of the neutral line and of plasmoids (Escoubet et al., 2001). Figure 2-1 shows a schematic of the Cluster orbit when it passed the apogee in the magnetotail.

### 2.1 Data sets used in this study

Each Cluster spacecraft carries eleven instruments package to measure the magnetic and electric field, and to detect the electron and ion distribution functions. In this study, magnetic field data from the Flux-Gate Magnetometer (FGM) (Balogh et al., 1997, 2001), thermal electron data from the Electron Drift Instrument (EDI) (Paschmann et al., 2001), electron velocity distributions from the Plasma Electron and Current Experiment (PEACE) (Johnstone et al., 1997), suprathermal electron data from the imaging energetic particle spectrometer (RAPID) (Wilken et al., 2001), and ion velocity integrated from ion distribution functions from the Cluster ion spectrometry (CIS) (Reme et al., 2001) are used. Table 2.1 summarizes the measurement ranges and the time resolutions from each instrument. The critical data that enable us to view sharp electron changes within DPFs that only 1-2 s front durations are obtained from the EDI electron measurements with sub-second

time cadence.

**Flux-Gate Magnetometer (FGM):** The Flux-Gate Magnetometer (FGM) carries out measurements of the DC magnetic field with two triaxial flux-gate sensors and via an on-board Data-Processing Unit (DPU). The magnetic field is an important characteristic of the plasma in the near-Earth environment as it allows insight into the structure of and processes occurring within the plasma during events of magnetospheric phenomena. The main objective of the FGM is to accurately detect the magnetic field from four Cluster spacecraft (Balogh et al., 1997). The measurement range of FGM in the near neutral sheet is  $\pm 64$  nT and the time resolution is 44.6 ms in the nominal mode and 14.9 ms in the burst mode (Balogh et al., 2001).

**Electron Drift Instrument (EDI):** Sub-second time resolution electron data used in this study come from the EDI (Paschmann et al., 2001). High time-resolution ambient electrons are measured by EDI with electrostatic analyzers in its ambient mode (16 sample/s in nominal mode and 128 sample/s in burst mode), and the electric-field mode (8 sample/s) as a by-product when no return beams are detected. In the ambient mode, no electrons are emitted and the instrument is used as a fast particle detector of electrons at pitch angles 0, 90 and 180 degrees. In this mode the two look directions are always antiparallel to each other. Various submodes determine which pitch angles are sampled, 90 degrees, or 0 and 180 degrees, or all three, and in the latter case also at which rate the switching between 90 degrees and 0 (180) degrees is done. The highest pitch angle switching rate is 16 Hz. This rate was used from November 25, 2005 onwards. The sampling duration is 16 ms in nominal mode and 8ms during burst mode intervals.

**Plasma Electron and Current Experiment (PEACE):** The PEACE instrument is designed to measure the electron velocity distribution in the vicinity of Cluster, covering an energy range of 0.7 eV to about 26 keV and detecting electrons arriving from all possible directions (i.e.  $4\pi$  steradian of solid angle) (Johnstone et al., 1997). PEACE consists of two sensors, a Low Energy Electron Analyzer (LEEA) and a High Energy Electron Analyzer (HEEA), which are mounted on opposite sides of the spacecraft with radial fields-of-view. LEEA and HEEA measure

different overlapping energy range, 0.7 eV to 1 keV and 30 eV to 26 keV, respectively. Each sensor has a field-of-view of  $180^\circ$  in the polar direction, consisting of twelve  $15^\circ$  zones. The azimuthal period indicates the spin of the satellite. Therefore, these sensors scan the 3D distribution in half a spacecraft rotation or 2 s where the energy ranges overlap (Szita et al., 2001; Owen et al., 2001). This provides a time resolution of 2 s. For those parts of the energy range covered by only one sensor, the time resolution is one spin period or 4 s. (Johnstone et al., 1997)

**Research with Adaptive Particle Imaging Detectors (RAPID):** The RAPID spectrometer is an advanced particle detector for the analysis of suprathermal plasma distributions in the energy range from 20-400 keV for electrons, 40-1500 keV (4000 keV) for hydrogen, and 10 keV/nuc-1500 keV (4000 keV) for heavier ions. Novel detector concepts in combination with pin-hole acceptance allow the measurement of angular distributions over a range of  $180^\circ$  in polar angle for either species. The detection principle for the ionic component is based on a two-dimensional analysis of the particle's velocity and energy.

**Cluster Ion Spectrometry (CIS):** The role of the Cluster Ion Spectrometry (CIS) experiment (Reme et al., 2001) is to measure the full, three-dimensional velocity distribution function of ions with a time resolution of 4 s (one spin period). Each CIS instruments was originally mounted on all 4 spacecraft but only three were operated on SC1, SC3 and SC4. CIS consists of two complementary sensors: the Hot Ion Analyzer (HIA) and the COmposition and DIstribution Function (CODIF) analyzer. HIA has the better angular resolution but does not offer mass resolution. The energy range of HIA is from  $\sim 5$  eV/e to 32 keV/e. CODIF measures the ion distribution functions of  $H^+$ ,  $He^{++}$ ,  $He^+$ , and  $O^+$  with an energy range of 0 to 40,000 energy per charge (eV/e).

Table 2.1: Summary of the measurement range and the time resolution of the Cluster instruments.

<b>Instrument</b>	<b>Measurement range</b>	<b>Time resolution</b>
FGM	-64 nT to +64 nT	44.6 ms / 14.9 ms
EDI	0.5 or 1 keV	0.125 s / 62.5 ms / 7.8 ms
PEACE	0.59 eV to 26.4 keV	2 s
RAPID (electron)	20-400 keV	4 s
CIS (HIA)	$\sim 5$ eV/e to 32 keV/e	4 s
CIS (CODIF)	$\sim 40$ eV/e to 40 keV/e	4 s



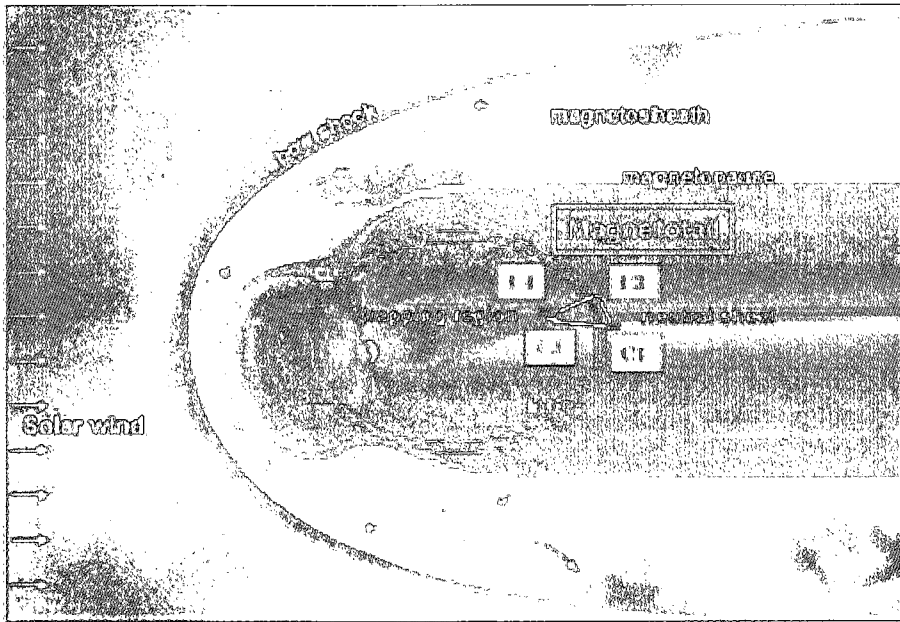


Figure 2-1: Schematic of the Cluster polar orbit when it passed the apogee ( $19.6 R_e$ ). The red line indicates the polar orbit of Cluster. When Cluster passed the apogee in the magnetotail, it was able to observe the DPFs. (taken from <http://sci.esa.int/>)

# CHAPTER 3

## RESULTS

Results of this study are discussed in this chapter. The selection criteria for the DPFs are described in section 3.1 and one example of the DPFs selected from those criteria is presented in section 3.2. The unique contributions of this study consist of two parts which are given in section 3.3 and section 3.4, respectively. One concerns the electron transitions from EDI, PEACE and RAPID at the DPFs, while the other looks at the propagation characteristics of DPFs using multi-point analysis of Cluster data.

### 3.1 Selection criteria

This section presents the selection criteria used to find events based on typical properties of DPFs, the abrupt increase of the  $B_z$  component, fast ion flows and decrease of the ion density as described in Figure 1-4. Based on these three criteria, 9 dates of event are selected during July to October when the apogee of Cluster was located in the magnetotail side from 2001 to 2007. The 9 dates of event are summarized together with the position of spacecraft 1 (SC1) in GSM coordinate in table 3.1. Each date of event includes several DPF events, hence, there are 24 DPFs from 9 dates. All spacecraft positions are projected in X-Y and X-Z planes in Figure 3-1. Each dot plots the spacecraft position with the different colors representing differing events. The Cluster orbit does not cover -6 to -10  $R_e$  from 2001 to 2007. The events on 20021002, 20021026, 20030919, 20051003, and 20071027 took place on the dusk-side, while the other events on 20060820, 20060903, 20070831, 20070907 were observed on the dawn-side. In this chapter examples of the electron transitions and the propagation characteristics of the DPFs during the 20051003 and 20060903

events are presented.

### 3.2 Example of the DPFs on 20051003

Figure 3-2 shows an example of the DPFs from 11:21:00 to 11:33:00 UT that took place on 20051003. The Cluster spacecraft was located in the near-equatorial plasma sheet (shown in Figure 3-1). The relative positions of the four spacecraft in X-Y plane and X-Z plane at 11:21:00 UT are shown in Figure 3-2(a). Compared with the other spacecraft, spacecraft 1 (SC1) is located near the current sheet center based on small values for  $B_y$  and  $B_x$ .  $B_z$  from FGM, density and velocity of  $H^+$  from CODIF on SC1 versus time on the X-axis are represented in Figure 3-2(b). All three components of the magnetic field measured by the four spacecraft are plotted in 3-2(c). If  $B_x$  is positive (negative), the spacecraft is located above (below) the current sheet. From this, it can be concluded that all spacecraft are located above the current sheet except for SC2. Furthermore, a larger  $B_x$  component on SC4 when compared to SC3 indicates that SC4 is above SC3, consistent with the relative positions of the spacecraft in 3-2(a). Based on  $B_x$  from SC2, SC2 is below the current sheet from at 11:21:00 and moves close to the current sheet after  $\sim 11:25:00$  UT. From these three plasma factors in 3-2(b), two typical DPFs are identified. The first DPFs started at 11:22:30 UT, up to 18 nT, and then came back to quiet mode at 11:23:50 UT. The second DPF was detected at 11:27:00 UT. Both DPFs show a sudden  $B_z$  rise with strong earthward ion flows as well as decrease of ion density. The ion density and velocity recovered back to the pre-DPF value after the first DPF. However, the ion density showed a lower value after second DPF. The earthward ion flows are observed after second DPF then steadily shown the positive  $V_x$ .

### 3.3 Electron transitions at the DPFs

In this section, the high time resolution electron data are presented to resolve the electron transition within the sudden  $B_z$  ramp at the DPFs. Figure 3-3(a) presents

samples of the electron distribution functions from PEACE. The PEACE data are plotted in log energy and pitch angle polar coordinate with  $0^\circ$  pitch angle at the top and  $180^\circ$  at the bottom of the plot. The phase space density ( $f_e$ ) in  $\text{s}^3/\text{km}^6$  is plotted in a color. The dashed circles on the plots indicate constant energies. In each distribution, data are shown in two snapshots in the left and right halves of the circles and the time when the two snapshots were taken is shown. The two snapshots were taken 2 s apart from each other (Chen et al., 2008). The DPF and post-DPF distributions are hotter and more tenuous than the distributions in the quiet-time current sheet, and therefore it is named the hot current sheet electron distribution in this study. Plotted above the magnetic field profiles observed by SC1 in Figure 3-3(b), the electron distribution is shown to be of the quiet-time current sheet type in the pre-DPFs and hot and tenuous in the post-DPFs.

The electron transitions observed by SC1 on 20051003 are presented in Figure 3-4(a). The figure shows the  $B_z$  profiles, thermal electrons from EDI (1 keV, 90-degree pitch angle, 8 sample/s) with the curve showing smoothed data (averaged over 151 samples) and suprathermal electrons (4 s per sample) from RAPID. The count of EDI electrons shows a sudden drop at the point in time when  $B_z$  rises and a gradual increase before the rise in  $B_z$  takes place for both DPFs. The fluxes of suprathermal electrons start to increase about 1 minute prior to the first sudden  $B_z$  rise. The energy dependent electron transition is similar to previous study shown in Figure 1-5 (Lui et al., 1992). The fluxes of lower-energy suprathermal electrons start to increase earlier than those of the higher-energy ones, indicating that the early enhancements of suprathermal electrons are not due to their large gyroradius (otherwise higher energy electrons would enhance earlier). The suprathermal electron flux level after the first DPF is significantly higher than the pre-DPF level. In order to resolve the electron transition in detail, a zoom-in view of the first DPF on 20051003 is presented in Figure 3-4(b). The electron counts start to decrease at the ramp of  $B_z$  rise but do not change before the increase of  $B_z$  takes place. The four consecutive PEACE electron distribution frames are labelled I, J, K, and L. Panel I shows the same features as the pre-DPF electron distributions, and J shows a slight decrease of perpendicular electrons. A hotter and more tenuous distribution than the quiet

current sheet distributions is shown in K, while L represents a hot and tenuous distribution in the region of large magnetic fluctuations following DPFs. The counts of electrons from EDI shows a decrease at 11:22:33 UT, while the PEACE electron distribution J (at 11:22:33.489-33.613 UT) indicates a slight drop in the phase space density of 90-degree electrons. During the  $B_z$  rise phase, the electron counts decrease in line with a decrease of phase space density from PEACE and finally, after the peak in  $B_z$ , the electron counts decrease to zero.

Figure 3-5 represents the electron transition occurring at the second DPF on 20051003. The time duration of the  $B_z$  rise at the second DPFs is 1.8 s and is similar to the typical DPF observed by THEMIS (Runov et al., 2009). Three components of the magnetic field (a) and 1-keV electron counts from EDI on SC1 and 500-eV electron counts from EDI on SC2 (b) are presented for 40 sec (Figure 3-5). In addition, an array of electron distribution functions from PEACE are shown in Figure 3-5(c). From top to bottom, PEACE data detected by SC4, SC3, SC1, and SC2 in the order of the  $z$  (GSM) projections of the spacecraft positions are presented. The electron transition occurred at about the same time as the sharp electron counts decrease on SC1 and SC2 (3-5(b)). The second DPF on 20051003 has a subsequent DPF on all spacecraft and the electron counts from EDI are correlated with this subsequent DPF. After the DPF observed at 11:26:14 UT, the counts of electrons increased for a short time and decreased again at the subsequent DPF on SC1. Considering that the snapshots of PEACE were taken every 2 s, the recovery of electron counts on SC1 cannot be recognized in detail from PEACE on SC1. However, this recovery of electron counts can be shown using EDI data for SC2 as well as PEACE data from SC2. The counts of electrons from EDI on SC2 decreased at the DPF at 11:26:58 UT and the slightly hotter electron distribution function detected by PEACE at 9.469 s (11:26:59.469 UT) after 11:26:50 UT as shown by the time marked at the corners of the thumbnail distributions in the array. Before the subsequent DPF, the counts of electrons then recovered and decreased again at 11:27:12 UT. The electron distributions show a hotter and more tenuous feature starting at 23.907 s (11:27:13.907 UT) according to the time given in PEACE array. The electron transitions are also observed from the PEACE on SC3 and SC4 at

DPF at 11:27:12 UT although there were no EDI data from SC3 and SC4 for this event.

Figure 3-6 shows the typical type of  $B_z$  rise as observed in previous studies (Ohtani et al., 2004; Runov et al., 2009; Lui et al., 1992) as well as two additional types found in this study. The enhancement of electron counts occurs at the  $B_z$  dip at 21:56:19 UT (Figure 3-6 (a)). The counts of electrons are decreased within the ramp of  $B_z$ . The counts of electrons are enhanced at the point of  $B_z$  dip. The electron density is a factor of the plasma pressure and  $B_z$  is a proxy of the magnetic pressure. The sum of the plasma pressure and the magnetic pressure tends to maintain constant when there is total pressure balance. A small dip in  $B_z$  implies a decrease in the magnetic pressure and an increase in the plasma pressure, indicating a plasma compression before DPFs. This observation is consistent with previous studies (Ohtani et al., 2004; Runov et al., 2009). Two additional types of  $B_z$  rise are described in Figure 3-6 (b) and (c), respectively. In contrast to the other observations, the second type (b) of  $B_z$  rise in Figure 3-6 has no  $B_z$  dip prior to the  $B_z$  rise. From this, it can be concluded that the tearing instability in the reconnection exhaust is not required to generate DPFs. The third type (c) of  $B_z$  rise has a break between the preceding  $B_z$  dip and sudden  $B_z$  rise. Among 24 DPFs examined in this study, a total of 16 DPFs belongs to (a) type and 7 (b) type and only one (c) type are observed. The decrease of plasma density after the DPFs is similar to the results from previous studies (Ohtani et al., 2004; Sergeev et al., 2009; Sitnov et al., 2009; Lui et al., 1992).

### 3.4 Propagation characteristics of the DPFs

The interest with propagations of DPFs has been growing because the fast earthward flows associated with DPFs are closely related to substorm activities. In order to investigate the direction of propagation, a multi-point analysis of Cluster is used in this study. First of all, it is necessary to define the arrival time of the DPF on each spacecraft. Figure 3-7 shows how the arrival time of DPF was derived using information on  $B_z$  peak or the lowest electron counts from EDI after the DPF on

20051003 in the dusk-side. The PEACE data are sometimes used to define the arrival time if the spacecraft does not have EDI data (PEACE data not shown in this figure). Three components of the magnetic field and counts of electrons at DPF are shown in Figure 3-7(a). The vertical line indicate the arrival time on each spacecraft. Figure 3-7(b) represents the zoom-in views of the magnetic field and counts of the electron data around the arrival time on SC1 and SC2. Based on the counts of electrons from EDI, the arrival time of DPF is 11:26:59 UT and 11:27:04 UT on SC1 and SC2, respectively. However, no EDI data for SC3 and SC4 for this date were available and hence, the arrival time on SC3 and SC4 was derived by using  $B_z$  peaks because when the counts of electrons are lowest on SC1 and SC2, the value of  $B_z$  shows a peak. The inferred arrival time on SC3 and SC4 is 11:27:13 and 11:27:13.2 UT, respectively. Therefore, the order of the DPF arrival is SC2, SC1, SC3, and SC4 from earliest to last using timing analysis. 3-7(c) shows the relative position of each spacecraft in x-y and x-z plane. In order to examine the front orientation, Minimum Variance Analysis (MVA) (Sonnerup and Scheible, 1998) is used in this study. The MVA of the magnetic field allows the determination of the direction in which the standard deviation of the magnetic field component is minimized. This is a convenient and practical way of analyzing real data to determine the normal of a sharp boundary in the space plasma environment. The results of MVA on 20051003 are described in Table 3.2. Based on timing analysis and MVA, it can be concluded that the DPF has a curved structure in X-Z plane and propagates earthward. The ion skin depth,  $d_i$ , is  $\sim 500$  km in this event. Based on the position of the spacecraft in X-axis, the arrival time of DPF, the assumption of a planar structure, and the speed of DPF on 20051003 can be deduced.  $V_x$  of DPF is approximately  $63.782$  km/s,  $1070.1$  km/s and  $4145.75$  km/s from SC2 to SC1, from SC1 to SC3 and from SC3 to SC4, respectively. The  $V_x$  of DPF would be constant if the DPF had a planar structure and propagates earthward. However, the DPF structure is curved and this feature is consistent with the discrepant  $V_x$  deduced for various spacecraft pairs assuming a planar structure.

The propagation characteristic of the dawn event, 20060903 is also examined using the same method (Figure 3-8). It is similar to use lowest counts of electrons

from EDI to define the arrival of DPF on 20051003, the arrival time is deduced for SC1, SC2 and SC3. SC4 does not have EDI data, hence it has to be inferred from PEACE electron distribution and there is a 2 s error bar. Therefore, the arrival time of DPF on 20060903 is 21:56:10.3 UT (SC2), 21:56:15 UT (SC3), 21:56:21.4 UT (SC1), and 21:56:30 UT (SC4). The results from MVA on 20060903 is also shown in Table 3.2. Using timing analysis and MVA, the DPF is found to have a curved structure in X-Z plane. However, the plane of propagation is curved in X-Y plane in a manner similar to a saddle structure. The structure propagates toward the Earth. Based on the position of the spacecraft in X-axis and the arrival time of DPF, the  $V_x$  of DPF is 569.96  $km/s$ , 9.97  $km/s$  and 934.47  $km/s$  from SC2 to SC3, from SC3 to SC1 and from SC1 to SC4, respectively. Although SC3 and SC1 are closely located in the X-axis, the arrival time of DPF takes 6.4 sec from SC3 to SC1. It is also concluded that the DPF has a curved structure and moves earthward.



Table 3.1: 9 Dates of DPF events with the position of spacecraft 1 (SC1).

Date (YYYYMMDD)	Time (HH:MM)	X of SC1 (Re)	Y of SC1 (Re)	Z of SC1 (Re)
20071027	09:00 ~ 09:30	-10.54	5.46	-1.68
20051003	11:15 ~ 11:45	-15.28	4.5	-0.69
20030919	23:30 ~ 24:00	-17.46	3.71	0.46
20021026	09:30 ~ 10:00	-11.29	11.43	-0.37
20021002	21:20 ~ 22:00	-16.54	7.81	-0.05
20060820	15:50 ~ 16:20	-14.03	-6.82	3.42
20060903	21:40 ~ 22:10	-14.92	-3.91	1.75
20070831	10:10 ~ 10:50	-14.66	-5.2	2.05
20070907	12:35 ~ 13:05	-14.48	-3.56	1.67

Table 3.2: Minimum Variance Analysis results on 20051003 and 20060903 with Eigen values,  $\lambda_0$ ,  $\lambda_1$  and  $\lambda_2$ .

Date	SC	Arrival (UT)	$\hat{x}$	$\hat{y}$	$\hat{z}$	$\lambda_0$	$\lambda_1$	$\lambda_2$
20051003	SC2	11:26:59	0.87	-0.15	0.47	0.4	1.65	29.9
	SC1	11:27:04	0.96	0.19	-0.19	0.06	1.04	23.6
	SC3	11:27:13	0.79	0.18	-0.58	0.09	2.75	20.96
	SC4	11:27:13.2	0.6	0.29	-0.74	0.04	1.41	4.16
20060903	SC2	21:56:10.3	0.55	0.61	-0.57	0.32	4.27	38.95
	SC3	21:56:15	0.5	0.73	0.46	0.81	10.4	30.55
	SC1	21:56:21.4	0.74	-0.66	-0.14	0.18	4.08	66.72
	SC4	21:56:30	0.96	0.06	-0.25	1.12	12.84	95.16



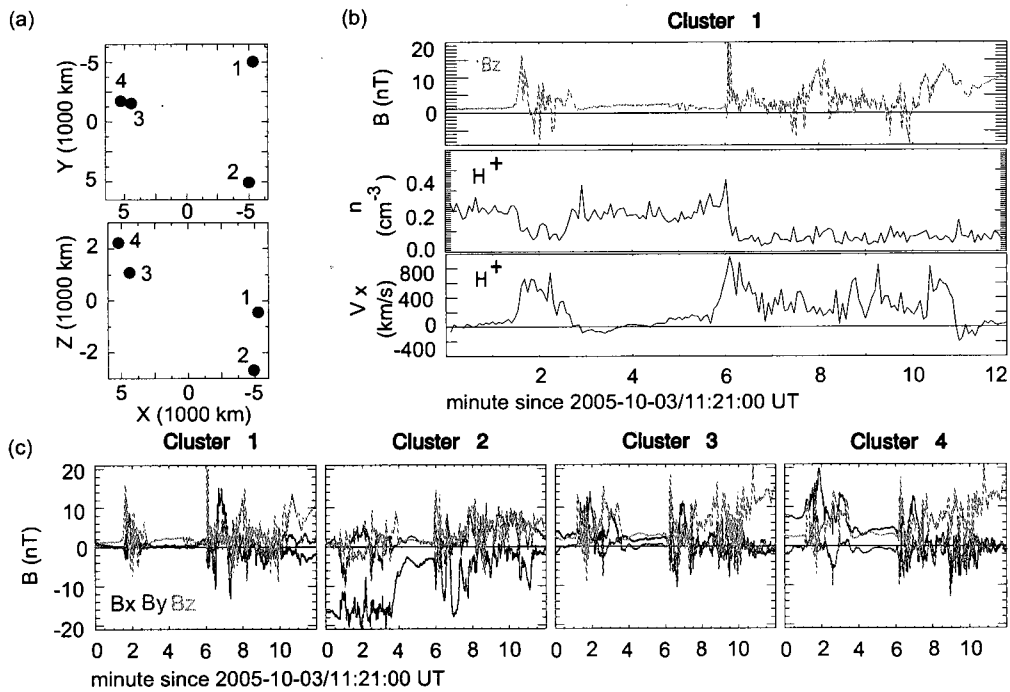


Figure 3-2: **Example of the DPFs on 20051003.** (a) Relative position of four spacecraft in x-y and x-z planes (GSM). (b) The z component of the magnetic field, density of  $H^+$ , and x component of the velocity of  $H^+$  detected by SC1. (c) Three components of the magnetic fields observed by all spacecraft.

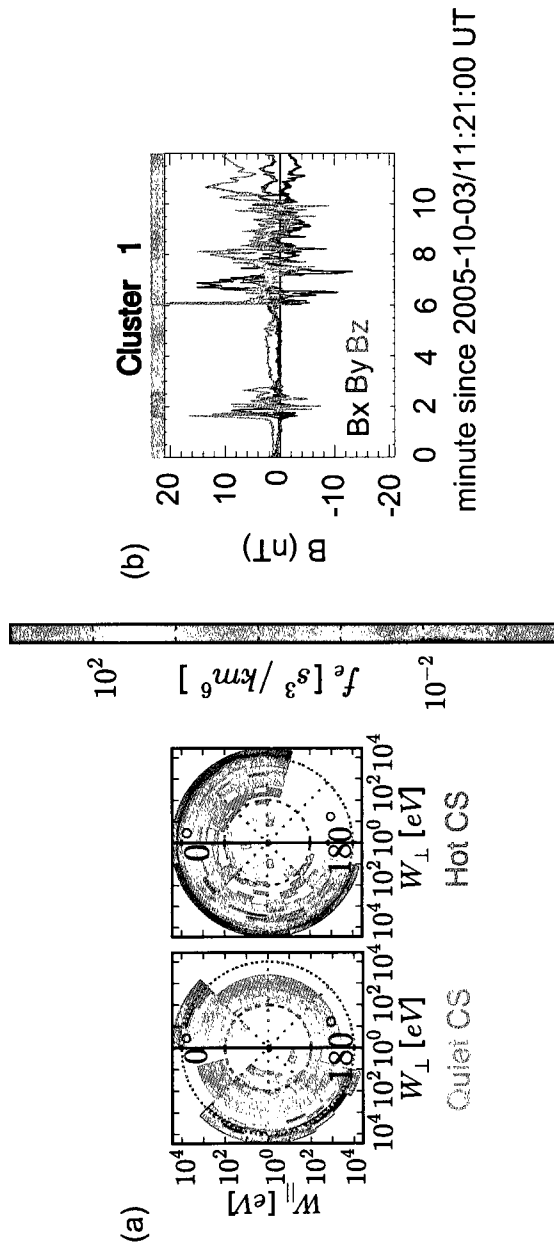


Figure 3-3: Samples of electron distribution functions from PEACE. Both the electron distribution in the quiet current sheet and the electron distribution in the hot current sheet are shown. The data are plotted in log energy and pitch angle polar coordinate with  $0^\circ$  pitch angle at the top and  $180^\circ$  at the bottom of the plot (a). The phase space density ( $f_e$ ) in  $s^3/km^6$  is plotted in color with the scale shown as a vertical bar. The dashed circles on the plots indicate constant energies. In the pre-DPFs, the electron distribution of the quiet-current-sheet type and in the post-DPFs the hot-current-sheet type are shown in (b) using data from spacecraft 1 as example.

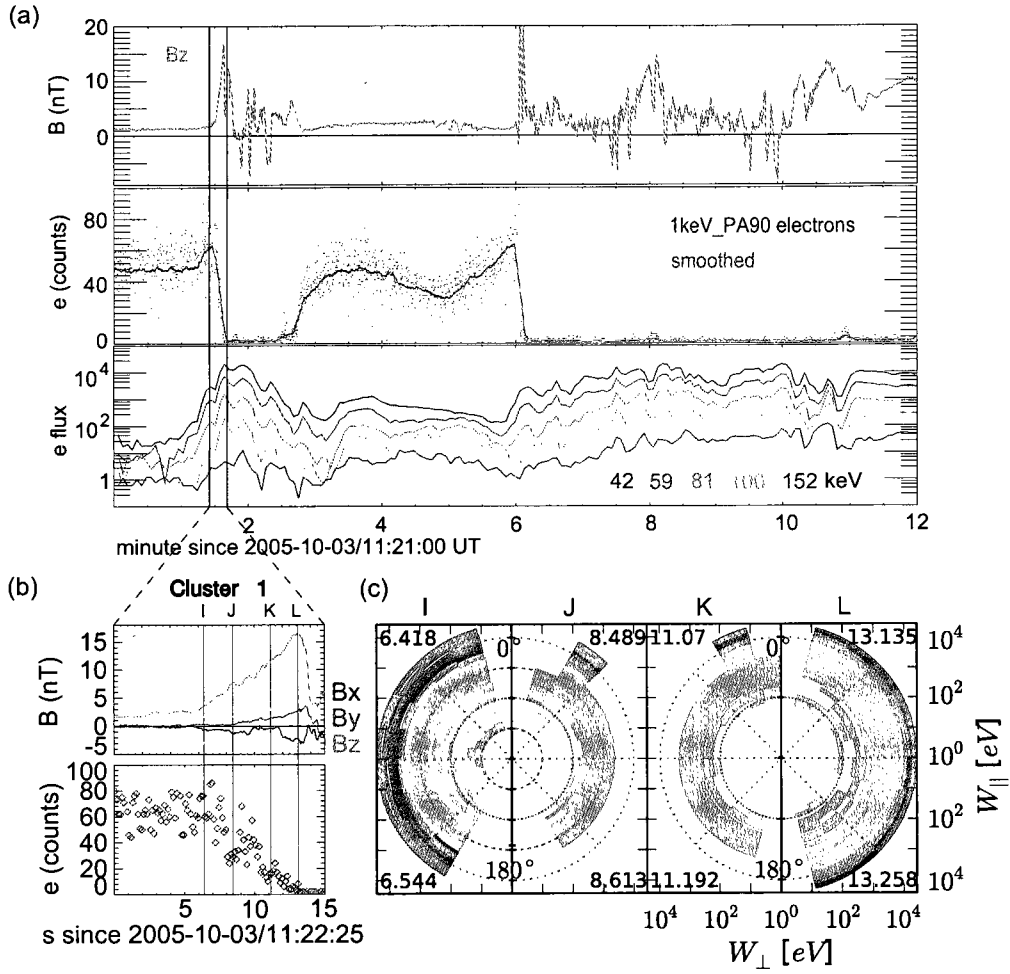


Figure 3-4: **Transitions of the thermal and the superthermal electrons on 20051003.** Time is shown on the x axis and is plotted versus  $B_z$  profiles, thermal electron data from EDI (1 keV, 90-degree pitch angle, 8 sample/s) with the curve showing smoothed data (averaged over 151 samples), and superthermal electron data (4 s per sample) from RAPID (a). The bottom panel (b) shows close-up data on electron transitions occurring at  $B_z$  rise of the DPFs. PEACE electron distribution functions are plotted in (c). Each vertical line is labelled alphabetically to indicate the time sequence at 6.418 s, at 8.489 s, at 11.07 s, and at 13.135 s since 11:22:25 UT on 20051003.

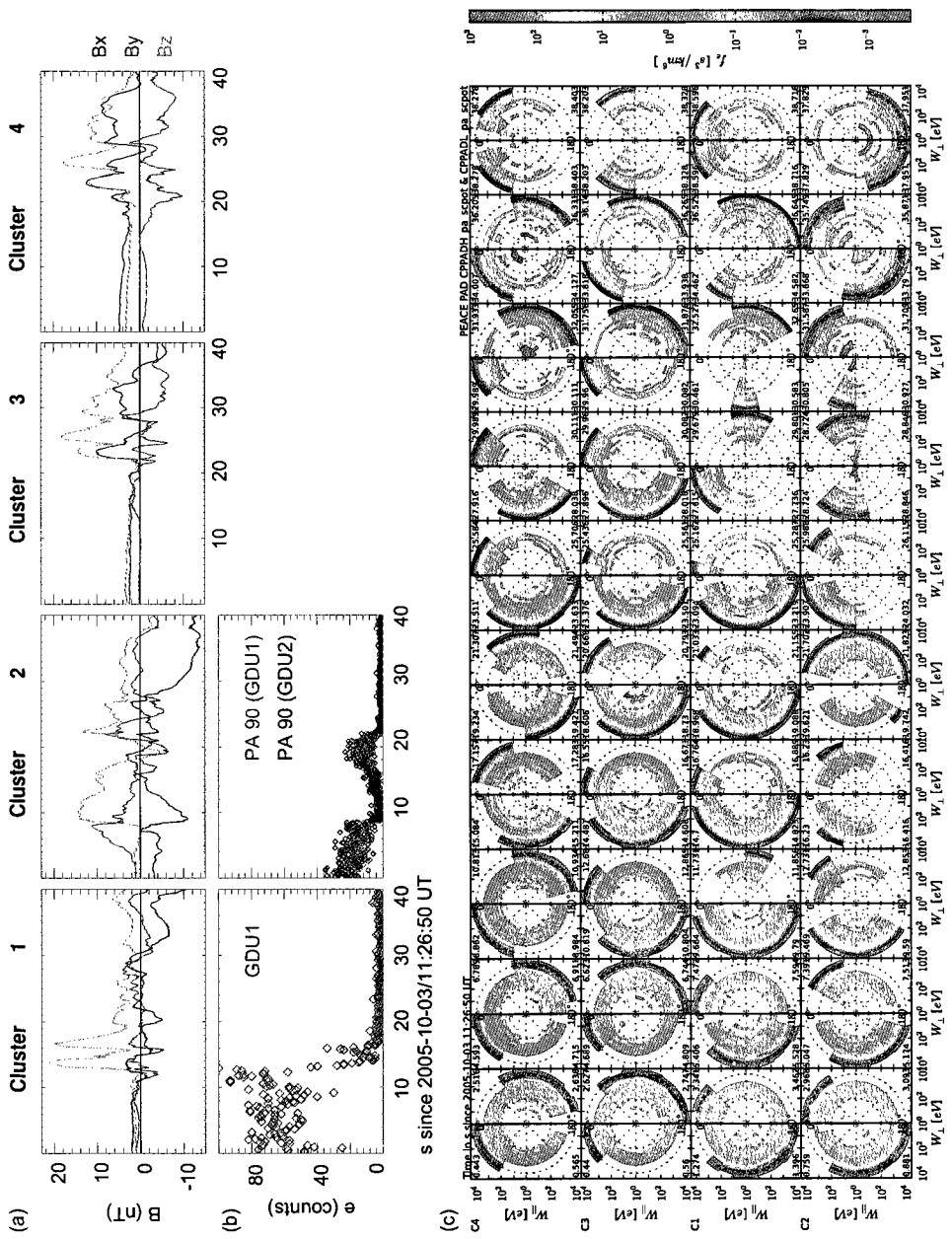


Figure 3-5: Electron transitions at the second DPF on 20051003. (a) Three components of the magnetic field from four spacecraft. (b) EDI electron data from SC1 (1 keV, 90-degree pitch angle, 8 sample/s) and from SC2 (500 eV, 90-degree pitch angle, 16 sample/s). (c) Array of electron distribution functions from PEACE showing the electron transition from top to bottom rows in the order of SC4, SC3, SC1, and SC2, according to the z projections of the spacecraft positions.

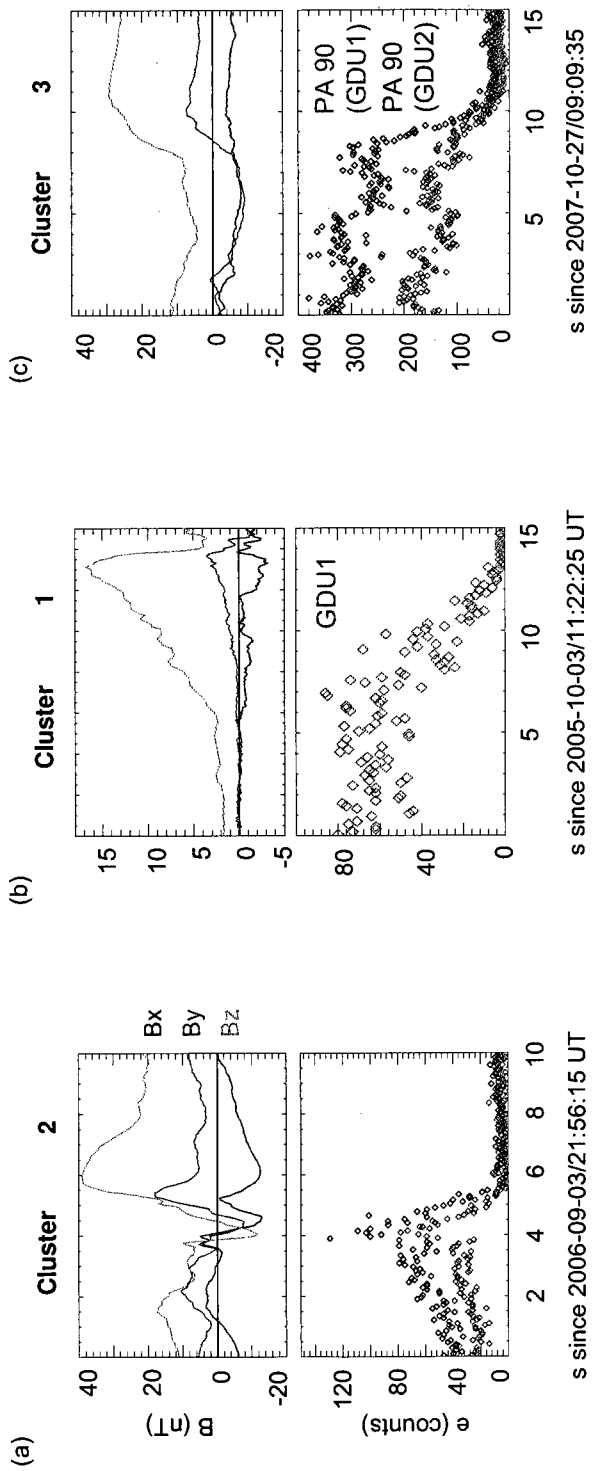


Figure 3-6: **Three types of  $B_z$  rise with electron transitions.** The typical type of  $B_z$  rise such as previously observed by Runov et al. (2009) is shown in (a). The second type of  $B_z$  rise without a small dip prior to  $B_z$  rise is presented in (b). The third type of  $B_z$  rise which shows a break between the small dip of  $B_z$  and the rise of  $B_z$  is shown in (c).

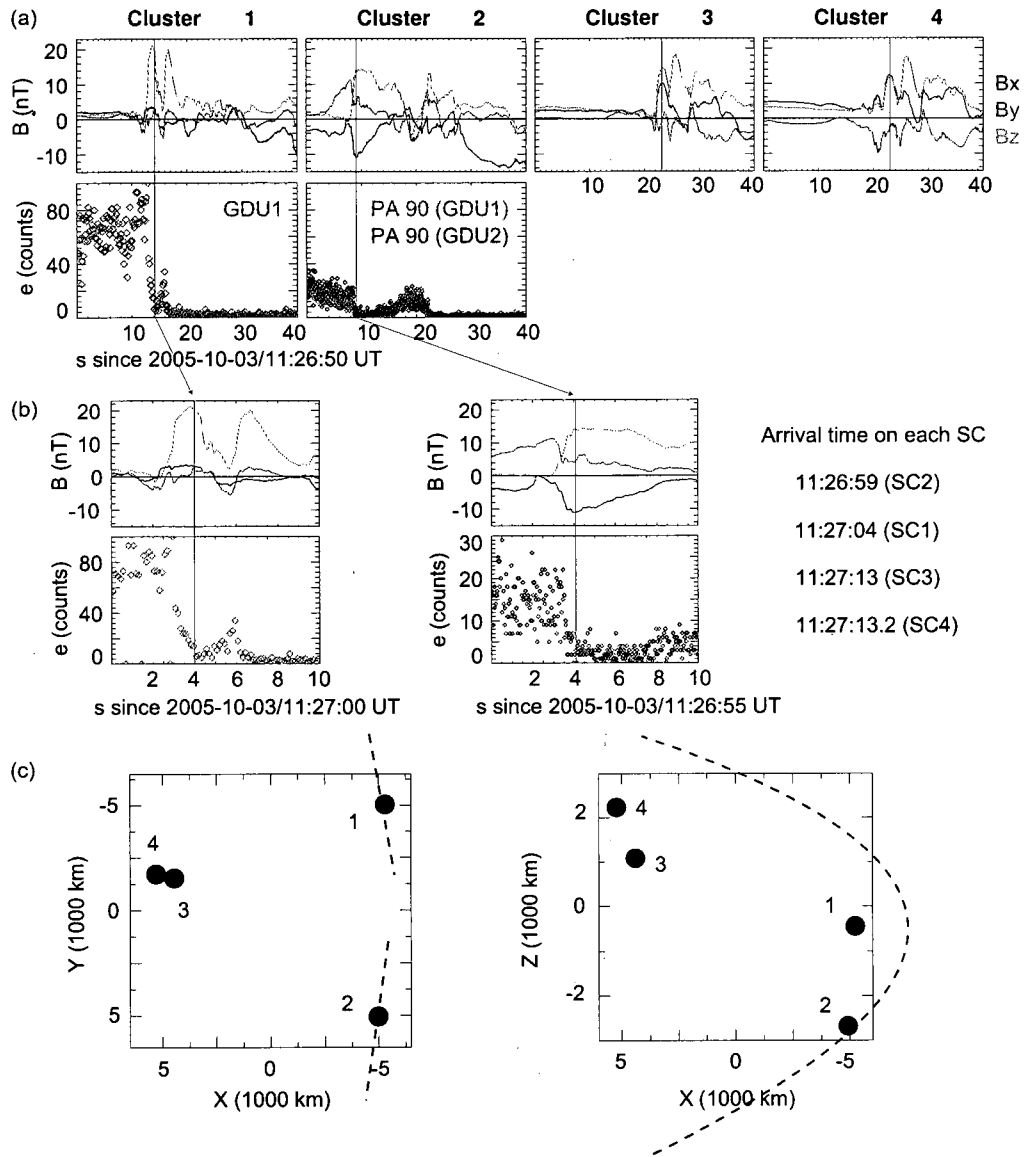


Figure 3-7: **Propagation characteristics of the DPF on 20051003.** Using  $B_z$  peak or the lowest counts of EDI electrons, the arriving time of the DPF was deduced for the 20051003 event at dusk-side. (a) Three components of the magnetic field from FGM and electron counts from EDI at DPF. (b) Zoom-in view of the magnetic field and EDI electron data on SC1 and SC2. (c) Relative position of 4 spacecraft in x-y (left) and in x-z (right) planes in GSM. Each vertical line indicates the arrival time on each spacecraft. The dashed line indicates the inferred plane of propagation from MVA.



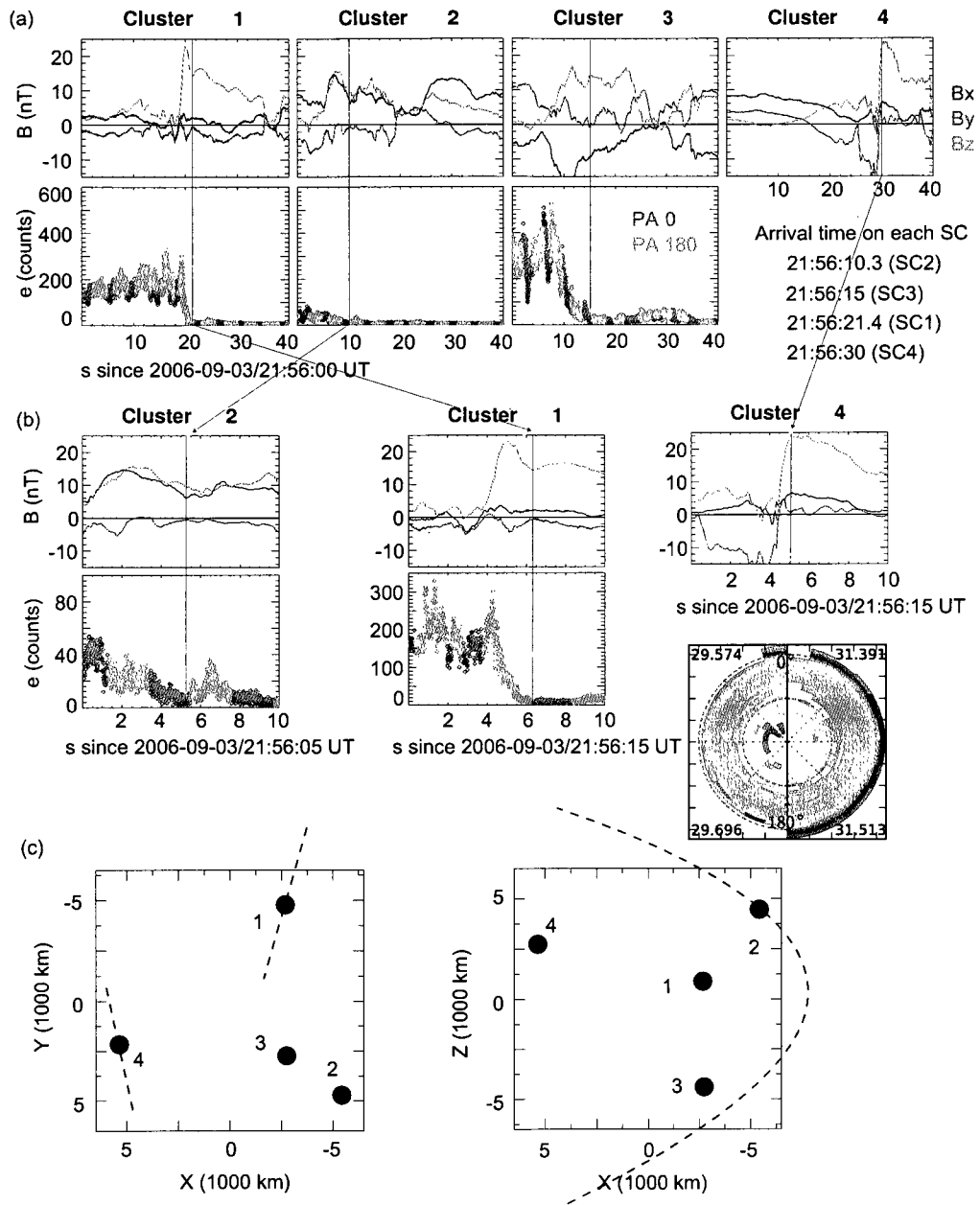


Figure 3-8: **Propagation characteristics of the DPF on 20060903.** Using the same method to define the arrival time, the propagation was deduced for the 20060903 DPF event in dawn-side. The same format as in Figure 3-7 is used. The magnetic field on SC4 with PEACE data showing the electron transition instead of EDI data on right panel of (b). Each vertical line indicates the arrival time on each spacecraft. The dashed lines indicate the inferred plane of propagation from MVA.

# CHAPTER 4

## DISCUSSION AND SUMMARY

In this thesis, the electron transitions with high time resolution data were addressed to resolve the  $B_z$  rise of DPFs. Furthermore, the propagation characteristics of DPFs were described using timing analysis and minimum variance analysis. The main results include:

1. The electron transitions occur at the ramp of  $B_z$  rise of the DPFs;
2. In some instances the  $B_z$  rise was found without a small dip prior to the sudden increase in  $B_z$ ;
3. Curved structures of DPFs propagate earthward.

As mentioned in the introduction, DPFs generated by the reconnection which produces the heated and accelerated injections are consistent with the DPF observation. In this section, two reconnection related models, the two fluid model (Ohtani et al., 2004) and the 2-D particle-in-cell (PIC) model (Sitnov et al., 2009), will be re-examined in light of the main results obtained in this thesis. Based on the two fluid simulation, the dipolarization can be produced by a fragmentation of a current sheet due to electron tearing instabilities. Figure 4-1(a) describes the magnetic X-lines produced by the instability with distributions of  $J_y$  in gray scale and with contours of the magnetic potential. The Earth is located in the left side of figure. The temporal evolutions of the plasma flow,  $B_z$  and plasma density from two virtual spacecraft in different positions ( $x = 42.4$  and  $52.4$ ) versus time are shown in Figure 4-1(b). The time and space scales are normalized by the inverse ion gyrofrequency,  $\Omega^{-1}$ , and ion skin depth,  $d_i = c/\omega_{pi}$ . The comparisons of the two-fluid simulation and the Cluster observation in this study are summarized as follows. The plasma velocities increase continuously in the simulation but the fast ion flows observed by

Cluster are localized in time at  $B_z$  jumps. Ohtani et al. (2004) noted that the transient fast plasma flows are caused by the reconnection that lasts for a limited time. The  $B_z$  profile in the simulation presents negative  $B_z$  that is as strong as the positive  $B_z$ , in contrary to a small dip of  $B_z$  prior to the increase from observations. This bipolar  $B_z$  structure in simulation is due to the magnetic island in between multiple X-lines in the current sheet. The plasma density has a sudden enhancement at the  $B_z$  reversal point in the simulation and decreases after  $B_z$  peak. In the Cluster observations, however, the enhancement of density occurs at the small dip of  $B_z$  as shown in Figure 3-6 (a).

The result of the 2-D PIC simulation is presented in Figure 4-2. The magnetic field lines and the color-coded current density,  $-J_y$ , at the moment  $\Omega_i t = 12$  is shown in the top panel and spatial profiles of the  $B_z$  at the  $z = 0$  plane at seven different moments,  $\Omega_i t$  are plotted in the bottom panel. The vertical dashed line indicates a sudden increase in  $B_z$ . The direction to the Earth is to the right side of figure. The  $B_z$  variation is positive (negative) at  $x > 0$  ( $x < 0$ ), hence the earthward (tailward) DPFs present the strong increase (decrease) of  $B_z$ . Sitnov et al. (2009) successfully produced the asymmetry of the south to north  $B_z$  profile of DPFs which was observed by Cluster in this study. Sitnov et al. (2009) described that the ion tearing instability in the exhaust is responsible for the generation of the DPF. However, some events in this study have no small dips of  $B_z$  prior to the sudden increase. This indicates that the tearing instability may not be necessary for the generation of DPFs. From what has been discussed above, it can be concluded that the PIC simulation result in Sitnov et al. (2009) is consistent with Cluster observations. However, their study does not describe the DPF without a small dip of  $B_z$ .

In this study, the electron transitions and the propagation characteristics of DPFs observed by Cluster are presented. The major results can be summarized as follows. (1) The electron transitions occur at the ramp of  $B_z$  rise of the DPFs. This result provides a new constraint on DPF generation models. As of yet, no models have made predictions on the electron transitions at DPFs. (2) In some cases,  $B_z$  rise did not show a preceding small dip prior to the sudden increase in

$B_z$ . This suggests that the tearing instability in the exhaust may not be required for the generation of DPFs. (3) Curved structures of DPFs propagate earthward. It is consistent with two simulations for the generation of the DPFs, although the curved structure is not described in the simulations. In conclusion, the observations presented in this thesis are consistent with the picture describing DPFs as injection fronts from reconnection exhaust.

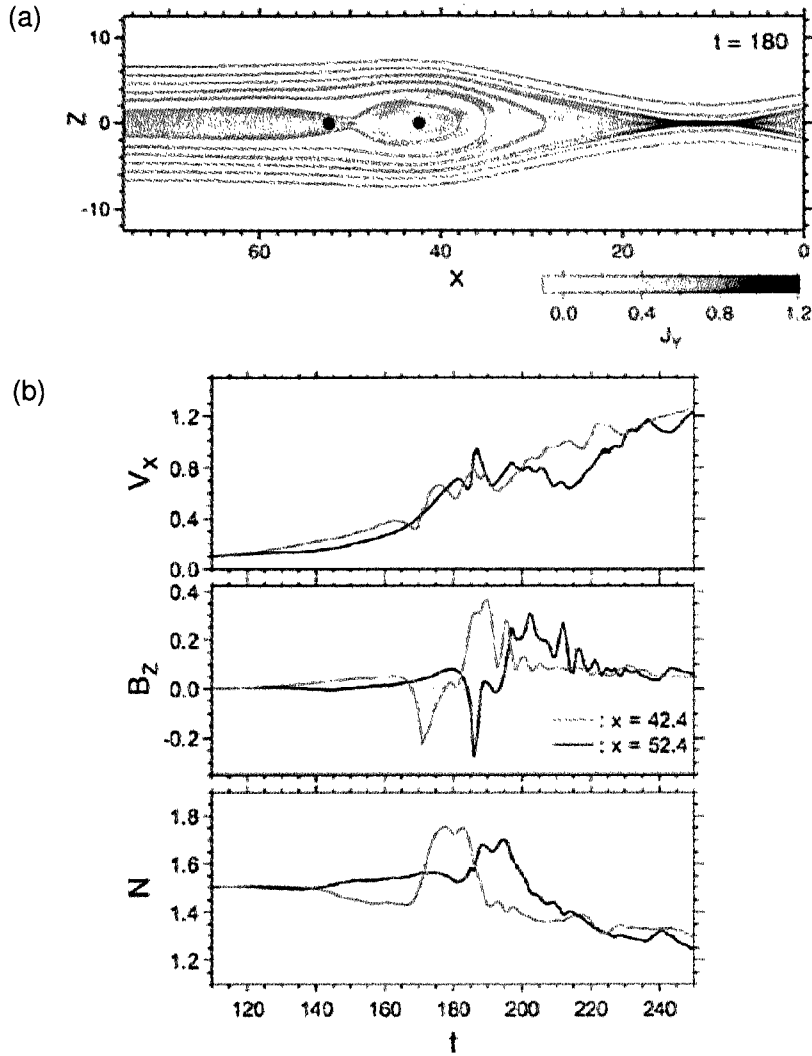


Figure 4-1: The generation of the DPF from two fluid simulation (Ohtani et al., 2004). Magnetic X-line with distribution of current density,  $J_y$ , in gray scale and with contours of the magnetic potential are plotted in (a). The Earth is on the left side of this Figure. From top to bottom, temporal evolution of the x component of plasma flow, the z component of magnetic field and the plasma density are shown in (b). Two different solid lines indicate the virtual spacecraft located in  $x=42.4$  and  $52.4$  in the simulation. The time and space scales are normalized by the inverse ion gyrofrequency,  $\Omega^{-1}$ , and ion skin depth,  $d_i$ .

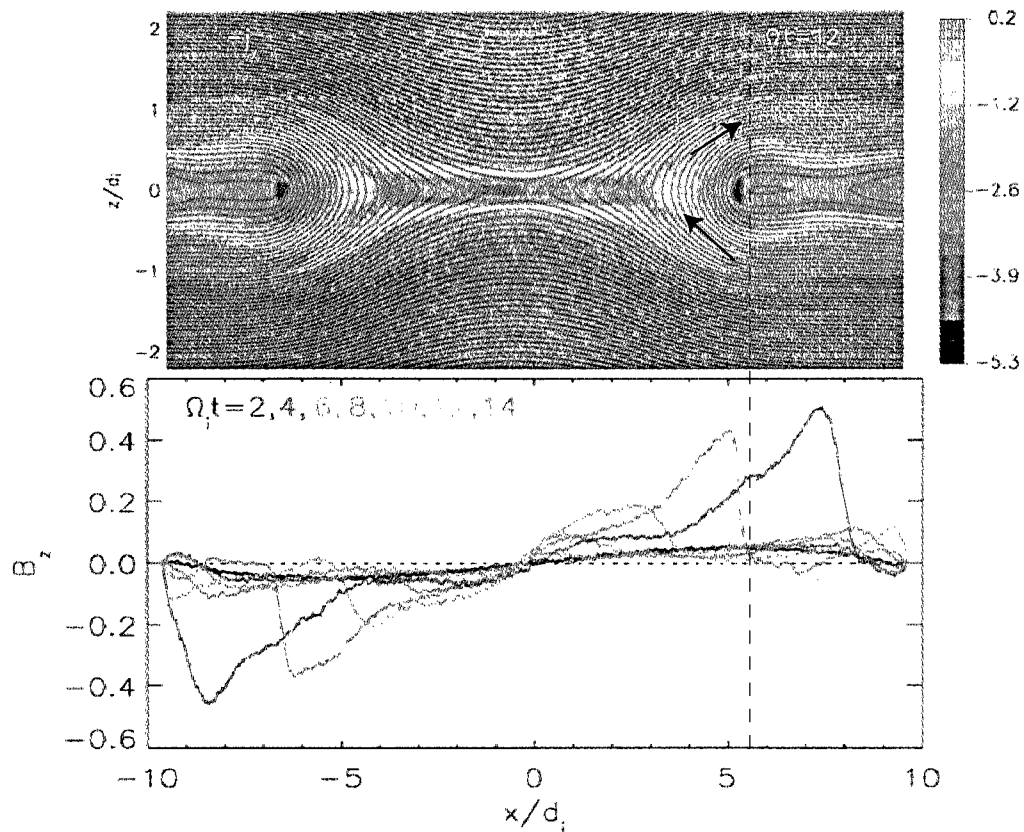


Figure 4-2: Magnetic field lines and the current density from 2-D PIC simulation (Sitnov et al., 2009). The top panel shows the magnetic field lines and the color-coded current density at the moment  $\Omega_i t = 12$ . The bottom panel presents the evolution of the  $B_z$  in  $z = 0$  plane at seven different moments. The vertical dashed line indicates the DPF at  $\Omega_i t = 12$ . The direction to the Earth is to the right.

## Bibliography

- Balogh, A., Carr, C., Acuna, M., Dunlop, M., Beek, T., Brown, P., Fornacon, K., Georgescu, E., Glassmeier, K., Harris, J., Musmann, G., Oddy, T., and Schwingschuh, K. (2001). The Cluster Magnetic Field Investigation: overview of in-flight performance and initial results. *ANNALES GEOPHYSICAE*, 19(10-12, Sp. Iss. SI):1207–1217.
- Balogh, A., Dunlop, M. W., Cowley, S. W. H., Southwood, D. J., Thomlinson, J. G., Glassmeier, K. H., Musmann, G., Luhr, H., Buchert, S., Acuna, M. H., Fairfield, D. H., Slavin, J. A., Riedler, W., Schwingschuh, K., and Kivelson, M. G. (1997). The Cluster magnetic field investigation. *SPACE SCIENCE REVIEWS*, 79(1-2):65–91.
- Chen, L. J., Bessho, N., Lefebvre, B., Vaith, H., Fazakerley, A., Bhattacharjee, A., Puhl-Quinn, P. A., Runov, A., Khotyaintsev, Y., Vaivads, A., Georgescu, E., and Torbert, R. (2008). Evidence of an extended electron current sheet and its neighboring magnetic island during magnetotail reconnection. *JOURNAL OF GEOPHYSICAL RESEARCH-SPACE PHYSICS*, 113(A12):A12213.
- Escoubet, C., Fehringer, M., and Goldstein, M. (2001). The Cluster mission - Introduction. *ANNALES GEOPHYSICAE*, 19(10-12, Sp. Iss. SI):1197–1200.
- Fillingim, M. O., Parks, G. K., Chen, L. J., and McCarthy, M. (2001). Comparison of plasma sheet dynamics during pseudobreakups and expansive aurorae. *PHYSICS OF PLASMAS*, 8(4):1127–1132.
- Hesse, M. and Birn, J. (1991). On Dipolarization and Its Relation to the Substorm Current Wedge. *JOURNAL OF GEOPHYSICAL RESEARCH-SPACE PHYSICS*, 96(A11):19417–19426.
- Johnstone, A., Alsop, C., Burge, S., Carter, P., Coates, A., Coker, A., Fazakerley, A., Grande, M., Gowen, R., Gurgiolo, C., Hancock, B., Narheim, B., Preece,

- A., Sheather, P., Winningham, J., and Woodliffe, R. (1997). Peace: A plasma electron and current experiment. *SPACE SCIENCE REVIEWS*, 79(1-2):351–398.
- Lui, A. T. Y., Lopez, R. E., Anderson, B., Takahashi, K., Zanetti, L., McEntire, R., Potemra, T., Klumpar, D., Greene, E., and Strangeway, R. (1992). Current Disruptions in the Near-Earth Neutral Sheet Region. *JOURNAL OF GEOPHYSICAL RESEARCH-SPACE PHYSICS*, 97(A2):1461–1480.
- Nakamura, R., Baumjohann, W., Klecker, B., Bogdanova, Y., Balogh, A., Reme, H., Bosqued, J., Dandouras, I., Sauvaud, J., Glassmeier, K., Kistler, L., Mouikis, C., Zhang, T., Eichelberger, H., and Runov, A. (2002). Motion of the dipolarization front during a flow burst event observed by Cluster. *GEOPHYSICAL RESEARCH LETTERS*, 29(20):2190.
- Ohtani, S., Shay, M., and Mukai, T. (2004). Temporal structure of the fast convective flow in the plasma sheet: Comparison between observations and two-fluid simulations. *JOURNAL OF GEOPHYSICAL RESEARCH-SPACE PHYSICS*, 109(A3):A03210.
- Owen, C., Fazakerley, A., Carter, P., Coates, A., Krauklis, I., Szita, S., Taylor, M., Travnicek, P., Watson, G., Wilson, R., Balogh, A., and Dunlop, M. (2001). Cluster PEACE observations of electrons during magnetospheric flux transfer events. *ANNALES GEOPHYSICAE*, 19(10-12, Part 2 Sp. Iss. SI):1509–1522.
- Paschmann, G., Quinn, J., Torbert, R., Vaith, H., McIlwain, C., Haerendel, G., Baner, O., Bauer, T., Baumjohann, W., Fillius, W., Forster, M., Frey, S., Georgescu, E., Kerr, S., Kletzing, C., Matsui, H., Puhl-Quinn, P., and Whipple, E. (2001). The Electron Drift Instrument on Cluster: overview of first results. *ANNALES GEOPHYSICAE*, 19(10-12, Sp. Iss. SI):1273–1288.
- Reme, H., Aoustin, C., Bosqued, M., Dandouras, I., Lavraud, B., Sauvaud, J., Barthe, A., Bouyssou, J., Camus, T., Coeur-Joly, O., Cros, A., Cuvilo, J., Ducay, F., Garbarowitz, Y., Medale, J., Penou, E., Perrier, H., Romefort, D., Rouzaud, J., Vallat, C., Alcaide, D., Jacquy, C., Mazelle, C., d’Uston, C., Mobius, E., Kistler, L., Crocker, K., Granoff, M., Mouikis, C., Popecki, M., Vosbury, M., Klecker, B., Hovestadt, D., Kucharek, H., Kuenneth, E., Paschmann, G., Scholer,



- M., Sckopke, N., Seidenschwang, E., Carlson, C., Curtis, D., Ingraham, C., Lin, R., McFadden, J., Parks, G., Phan, T., Formisano, V., Amata, E., Bavassano-Cattaneo, M., Baldetti, P., Bruno, R., Chionchio, G., Di Lellis, A., Marcucci, M., Pallochia, G., Korth, A., Daly, P., Graeve, B., Rosenbauer, H., Vasyliunas, V., McCarthy, M., Wilber, M., Eliasson, L., Lundin, R., Olsen, S., Shelley, E., Fuselier, S., Ghielmetti, A., Lennartsson, W., Escoubet, C., Balsiger, H., Friedel, R., Cao, J., Kovrazhkin, R., Papamastorakis, I., Pellat, R., Scudder, J., and Sonnerup, B. (2001). First multispacecraft ion measurements in and near the Earth's magnetosphere with the identical Cluster ion spectrometry (CIS) experiment. *ANNALES GEOPHYSICAE*, 19(10-12, Sp. Iss. SI):1303–1354.
- Runov, A., Angelopoulos, V., Sitnov, M. I., Sergeev, V. A., Bonnell, J., McFadden, J. P., Larson, D., Glassmeier, K. H., and Auster, U. (2009). THEMIS observations of an earthward-propagating dipolarization front. *GEOPHYSICAL RESEARCH LETTERS*, 36.
- Sergeev, V., Angelopoulos, V., Apatenkov, S., Bonnell, J., Ergun, R., Nakamura, R., McFadden, J., Larson, D., and Runov, A. (2009). Kinetic structure of the sharp injection/dipolarization front in the flow-braking region. *GEOPHYSICAL RESEARCH LETTERS*, 36.
- Sitnov, M. I., Swisdak, M., and Divin, A. V. (2009). Dipolarization fronts as a signature of transient reconnection in the magnetotail. *JOURNAL OF GEOPHYSICAL RESEARCH-SPACE PHYSICS*, 114(A4):A04202.
- Sonnerup, B. U. O. and Scheible, M. (1998). Minimum and Maximum Variance Analysis. in *Analysis Methods for Multi-spacecraft Data*, edited by G. Paschmann and P. Daly.
- Szita, S., Fazakerley, A., Carter, P., James, A., Travnicek, P., Watson, G., Andre, M., Eriksson, A., and Torkar, K. (2001). Cluster PEACE observations of electrons of spacecraft origin. *ANNALES GEOPHYSICAE*, 19(10-12, Part 2 Sp. Iss. SI):1721–1730.
- Volwerk, M., Lui, A. T. Y., Lester, M., Walsh, A. P., Alexeev, I., Cao, X., Dunlop, M. W., Fazakerley, A. N., Grocott, A., Kistler, L., Lun, X., Mouikis, C., Pu, Z.,

Shen, C., Shi, J. K., Taylor, M. G. G. T., Baumjohann, W., Nakamura, R., Runov, A., Voeroes, Z., Zhang, T. L., Takada, T., Reme, H., Klecker, B., and Carr, C. M. (2008). Magnetotail dipolarization and associated current systems observed by Cluster and Double Star. *JOURNAL OF GEOPHYSICAL RESEARCH-SPACE PHYSICS*, 113(A8):A08S90.

Wilken, B., Daly, P., Mall, U., Aarsnes, K., Baker, D., Belian, R., Blake, J., Borg, H., Buchner, J., Carter, M., Fennell, J., Friedel, R., Fritz, T., Gliem, F., Grande, M., Kecskemety, K., Kettmann, G., Korth, A., Livi, S., McKenna-Lawlor, S., Mursula, K., Nikutowski, B., Perry, C., Pu, Z., Roeder, J., Reeves, G., Sarris, E., Sandahl, I., Soraas, F., Woch, J., and Zong, Q. (2001). First results from the RAPID imaging energetic particle spectrometer on board Cluster. *ANNALES GEOPHYSICAE*, 19(10-12, Sp. Iss. SI):1355–1366.